Cobalt Imido Complexes | Hot Paper |

Umpolung in a Pair of Cobalt(III) Terminal Imido/Imidyl Complexes

Weiqing Mao, Dominik Fehn, Frank W. Heinemann, Andreas Scheurer, Maurice van Gastel, Sergio A. V. Jannuzzi, Serena DeBeer,* Dominik Munz,* and Karsten Meyer*

Abstract: Reaction of the Co^I complex [(TIMMN^{mes})Co^I](PF$_6$) (**1**) (TIMMN^{mes} = *tris*-[2-(3-mesityl-**im**idazolin-2-ylidene)-**m**ethyl]ami**n**e) with mesityl azide yields the Co^{III} imide [(TIMMN^{mes})Co^{III}(NMes)]-(PF$_6$) (**2**). Oxidation of **2** with [FeCp$_2$](PF$_6$) provides access to a rare Co^{III} imidyl [(TIMMN^{mes})Co(NMes)]-(PF$_6$)$_2$ (**3**). Single-crystal X-ray diffractometry and EPR spectroscopy confirm the molecular structure of **3** and its $S = \frac{1}{2}$ ground state. ENDOR, X-ray absorption spectroscopy and computational analyses indicate a ligand-based oxidation; thus, an imidyl-radical electronic structure for **3**. Migratory insertion of one ancillary NHC to the imido ligand in **2** gives the Co^I *N*-heterocyclic imine (**4**) within 12 h. Conversely, it takes merely 0.5 h for **3** to transform to the Co^{II} congener (**5**). The migratory insertion in **2** occurs via a nucleophilic attack of the imido ligand at the NHC to give **4**, whereas in **3**, a nucleophilic attack of the NHC at the electrophilic imidyl ligand yields **5**. The reactivity shunt upon oxidation of **2** to **3** confirms an umpolung of the imido ligand.
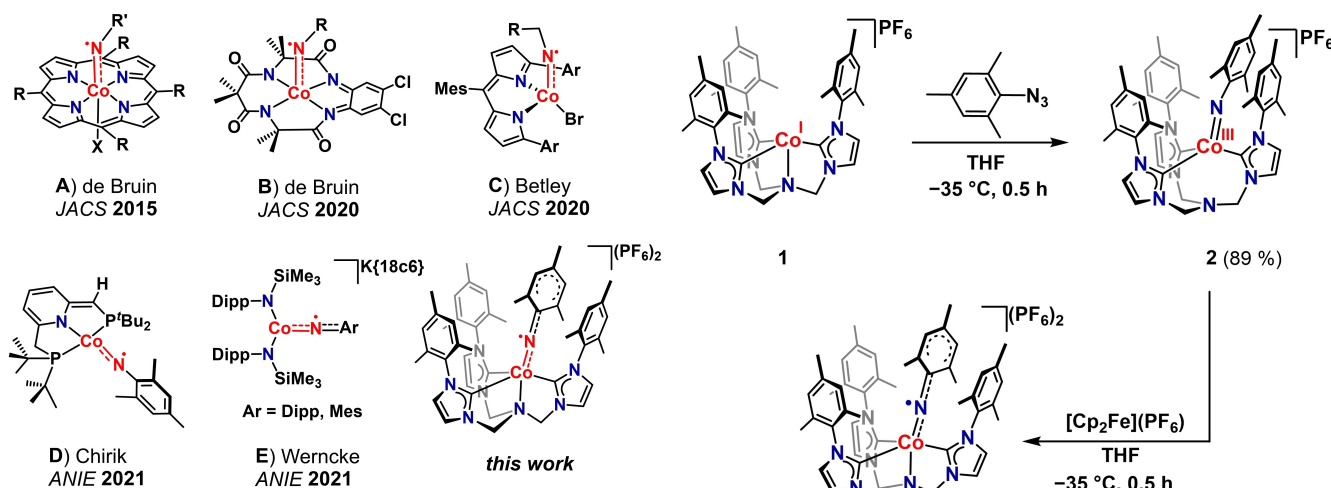
[*] Dr. W. Mao, D. Fehn, Dr. F. W. Heinemann, Dr. A. Scheurer, Prof. Dr. D. Munz, Prof. Dr. K. Meyer
Friedrich-Alexander-Universität Erlangen-Nürnberg (FAU), Inorganic Chemistry
Egerlandstrasse 1, 91058 Erlangen (Germany)
E-mail: karsten.meyer@fau.de

Prof. Dr. D. Munz
Current address: Saarland University, Inorganic Chemistry: Coordination Chemistry
Campus C4.1, 66123 Saarbrücken (Germany)
E-mail: dominik.munz@uni-saarland.de

Dr. S. A. V. Jannuzzi, Prof. Dr. S. DeBeer
Max Planck Institute for Chemical Energy Conversion
Stiftstr. 34–36, 45470 Mülheim an der Ruhr (Germany)
E-mail: serena.debeer@cec.mpg.de

Dr. M. van Gastel
Max-Planck-Institut für Kohlenforschung
Kaiser-Wilhelm-Platz 1, 45470 Mülheim an der Ruhr (Germany)

Introduction

Late 3*d* transition metal imido complexes are appealing synthetic targets as they are often implicated as critical intermediates in metal-catalyzed *N*-group-transfer chemistry.[1] These formal imides (R–N) could exist in a number of electronic formulations, including (*a*) "classic" closed-shell double- or triple-bonded, dianionic RN^{2-} ligands, (*b*) "imidyl" ligands with one unpaired electron residing at the imido ligand, or (*c*) a metal coordinating singlet- or triplet- "nitrene" with a formal electron-sextet at the nitrogen atom.

In general, the reactivity of late transition metal terminal imido complexes is controlled by the spin density at the imido ligand, the formal oxidation- and spin state of the metal ion, as well as its coordination number and geometry. The accumulation of spin density at the imido ligand is thought to be essential for high reactivity. Betley et al. have demonstrated that oxidation of the iron imido complex [(^{Ar}L)Fe(NAd)] (^{Ar}L = 5-mesityl-1,9-(2,4,6-Ph$_3$C$_6$H$_2$)-dipyrrin) to its imidyl redox isomer [(^{Ar}L)FeCl(•NAd)] results in a C–H amination rate enhancement of two orders of magnitude.[2] Examples of late transition metal imidyl/nitrene radical complexes, however, remain scarce, and structurally characterized examples in high oxidation states are even rarer. While formal Fe^{III} imidyl species are known,[2,3] considerably fewer metal imidyl/nitrene radical complexes of Co,[4] Ni,[5] and Cu[6] in mid to high oxidation states have been reported. For example, cobalt complexes with formal imido ligands have been structurally characterized, now, spanning various oxidation states and electronic structures (Co^{II} $S = 3/2$, $S = 1/2$;[7] Co^{II}(•NR) $S = 2$, $S = 1$;[4] Co^{III} $S = 0$, $S = 1$, $S = 2$;[7b,8] Co^{IV} $S = 1/2$;[8n,9] and Co^V $S = 0$[9]). Among them, low- to mid-valent Co^{II}[7] and Co^{III}[7b,8] imidos have been the subject of intensive studies. In contrast, reactive formal Co^{III} imidyl/nitrene radical complexes have been only proposed as transient intermediates (Figure 1, **A** and **B**)[10,12] or observed via single-crystal-to-crystal transformation (Figure 1, **C**).[13] Two investigations on formal Co^{II} imidyl radical species have been published in 2021 (Figure 1, **D** and **E**).[4] In sight of the few structurally authenticated nitrene- and imidyl-radical compounds, comparatively few is known about their reactivity in regard to isoelectronic carbenes and carbene radicals.[14] The homocoupling of nitrenes or the cross-coupling with carbene surrogates seems a convenient and complementary route to generate azo compounds[15] and imines.[16] In previous studies, we reported that TIMEN^{Ar}-supported Co^{III} imido species rapidly form Co^{II} bis(carbene) imine complexes by intramolecular migra-

Angew. Chem. Int. Ed. **2022,** *61,* e202206848 (1 of 9)

© 2022 The Authors. Angewandte Chemie International Edition published by Wiley-VCH GmbH

Figure 1. Reported (**A**–**E**) cobalt imidyl/nitrene radical complexes, including this work.

Scheme 1. Synthesis of target complexes [(TIMMN^{mes})Co^{III}(NMes)](PF$_6$) (**2**) and [(TIMMN^{mes})Co(NMes)](PF$_6$)$_2$ (**3**).

tory insertion of the imido group into one of the NHC pendant ligand arms.[8d]

The aforementioned prompted us to explore the electronic structure and migratory insertion chemistry of reactive, formal Co^{III} imidyl radical complexes supported by a recently developed, tripodal *N*-heterocyclic carbene (NHC) ligand. Employing the methylene-bridged, *N*-anchored tripodal NHC ligand (TIMMN^{mes}) has enabled the recent isolation and characterization of a Co^{IV} terminal alkylimido complex [(TIMMN^{mes})Co^{IV}(NAd)](OTf)$_2$ by our group.[8n] Note, the alkyl or aryl substituent (R) of the metal imido unit (NR) has been proposed as a crucial element manipulating the electronic structure.[8i,17]

In this context, we report herein a pair of Co^{III} terminal aryl imido/imidyl complexes, with the first example of a fully characterized Co^{III} imidyl radical, including its solid-state molecular structure. Both complexes show intramolecular migratory insertion of the imido- with an NHC ligand. However, whereas it proceeds through a closed-shell mechanism for the imide, it is mechanistically distinct for the imidyl species; thereby, involving the transfer of only one electron to the metal. Thus, this process is slow for the former but fast and efficient for the latter.

Results and Discussion

Treatment of the four-coordinate Co^{I} precursor [Co^{I}-(TIMMN^{mes})](PF$_6$) (**1**), prepared by reducing divalent [(TIMMN^{mes})Co^{II}(Cl)](PF$_6$)[8n] with sodium amalgam (1.2 equiv), with 1 equiv of mesityl azide in THF provided the green Co^{III} imide [(TIMMN^{mes})Co^{III}(NMes)](PF$_6$) (**2**) in 89% yield (Scheme 1).

Trivalent **2** is diamagnetic (d^6 low-spin, $S=0$), and the ^{1}H and ^{13}C NMR spectra reveal C_3 symmetry in solution. The TIMMN^{mes} ligand in **2** coordinates in a tridentate fashion and the amine anchor does not interact considerably with the cobalt ion (d(Co–N1)=3.236(2) Å). While the room temperature ^{1}H NMR spectrum of imido complex **2** is
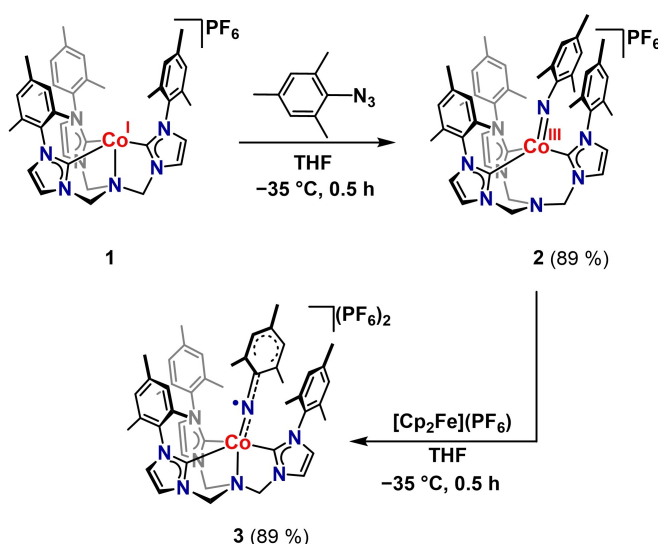
consistent with a C_3-symmetric structure, an unusually bent N(anchor)–Co–N(imido) moiety is observed in its solid-state molecular structure (Figure 2). The metrical parameters in **2** are consistent with a distorted seesaw geometry around the Co^{III} ion, composed of three carbon donors from the tris-carbene chelate and a fourth nitrogen ligand from the bound mesityl imido unit. The geometry index parameter τ_4 for **2** is 0.75, substantiating a seesaw geometry closer to tetrahedral ($\tau_4=1$) than to square planar limits ($\tau_4=0$).[18] As far as we are aware, this is the first of such a case in all cobalt imido complexes to be crystallographically studied.
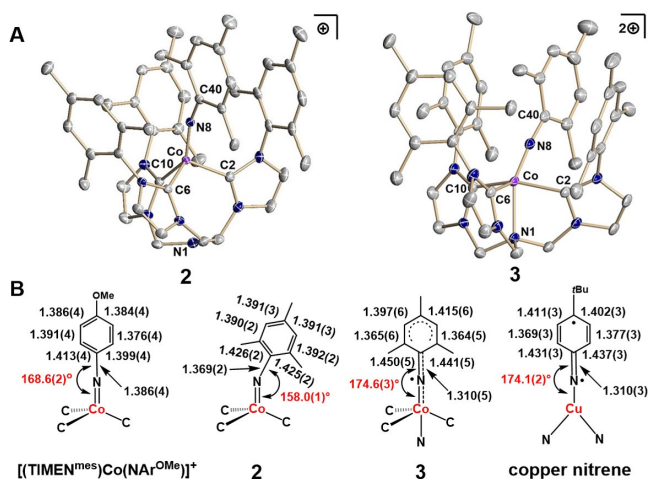
Figure 2. A) Molecular structures of the cation in crystals of [(TIMMN^{mes})Co^{III}(NMes)](PF$_6$) • 2 CH$_2$Cl$_2$ (**2**), and dication in crystals of [(TIMMN^{mes})Co(NMes)](PF$_6$)$_2$ • 5 C$_4$H$_8$O • 0.5 C$_5$H$_{12}$ (**3**). Hydrogen atoms and solvent molecules were omitted for clarity. Thermal ellipsoids are displayed at 50% probability. B) Core bond metrics of [(TIMEN^{mes})Co(NAr^{OMe})]$^+$,[8d] **2**, **3**, and copper nitrene [(^{EMind}L)Cu(N-(C$_6$H$_4$^{t}Bu))].[6]

The Co–N(imido) bond (d(Co–N8) = 1.677(1) Å) is within the range of previously reported Co^{III} aryl imidos (1.65–1.68 Å).[7b,8a,b,d,j] The N(imido)–C(mesityl) bond of 1.369(2) Å is significantly shorter than that of an N–C single bond (sum of the N and C covalent radii is 1.52 Å), suggesting a substantial degree of electron delocalization within the mesityl imido ligand.[1k] This situation is also observed in other structurally characterized Co^{III} aryl imido complexes.[7b,8a,b,d,j] Notably, the imido linkage in **2** deviates significantly from linearity [(Co–N(imido)–C(mesityl): 158.0(1)°] compared to other structurally authenticated Co^{III} aryl imido complexes (167.0–178.5°).[7b,8a,b,d,j] It is also important to note that one of the mesityl groups of the TIMMN^{mes} chelate is positioned nearly parallel to the mesityl group of the imido ligand, with a centroid-centroid distance of 3.70 Å and an interplanar angle of only 10.34°, indicating π–π interactions.[19] The deviation from linearity for the Co–N–C$_{Mes}$ linkages is either due to this interaction, crystal-packing effects, or implies considerable lone-pair character at the *N*-atom (see below).[5,20] Close inspection of the C–C bond lengths within the imido mesityl unit of **2** (Figure 2) reveals an elongation of the C$_{ipso}$–C$_{ortho}$ bonds (1.426(2), 1.425(2) Å), analogous to what has been observed for the closely related Co^{III} imido TIMEN derivative [(TIMEN^{mes})Co(NAr^{OMe})]$^+$ as well as for other Co^{III} aryl imido complexes.[7b,8a,b,d,j] Further unusual is the short distance between the imido nitrogen (N8) and one of the coordinated carbene carbon (C6) donors: the N8–C6 distance of 2.795 Å is considerably smaller than the sum of their van der Waals (VdW) radii (3.25 Å). Another remarkable feature is the trigonal planar, sp^2-hybridized amine *N*-anchor in **2**, with C–N–C angles summing up to 359.7(2)°, which closely resembles that of the previously reported [(TIMMN^{mes})Co^{III}(NAd)](BPh$_4$) (357.8°).[8n] The average C–N(anchor) bond (1.428(2) Å) in trivalent **2** also is significantly shortened compared with that in Co^I complex **1** (1.463(2) Å).

Cyclic voltammetry studies of **2** in THF revealed a reversible oxidation with $E_{1/2} = -0.52$ V vs. [FeCp$_2$]$^{0/+}$ (for details, see the Supporting Information). Accordingly, and in agreement with the electrochemical data, **2** is readily oxidized by [FeCp$_2$](PF$_6$) (Cp$^- = \eta^5$-C$_5$H$_5^-$) in a THF solution. Regardless, all attempts to isolate the oxidized complex at room temperature were complicated by the high reactivity of the target compound, as quantified by a half-life of fewer than 5 mins at 25 °C, according to UV/Vis electronic absorption spectroscopy. The UV/Vis spectrum of the oxidized product is distinctly different from that of **2**, with a broad band centered at $\lambda_{max} = 515$ nm ($\varepsilon = 2860$ M^{-1} cm^{-1}; Figure S11). While the product is thermally sensitive, it is sufficiently stable at low temperatures; thus, allowing for its isolation and characterization. Accordingly, brown [(TIMMN^{mes})Co(NMes)](PF$_6$)$_2$ (**3**) could be synthesized in 89 % yield from the precursor **2** by the reaction with 1 equiv of [FeCp$_2$](PF$_6$) at −35 °C (Scheme 1, bottom).

Dark brown crystals, suitable for SC-XRD analysis, were grown by slow diffusion of *n*-pentane into a THF solution of **3** at −35 °C. The cobalt center in **3** is located in a distorted, trigonal-bipyramidal environment of C_{2v} symmetry, with the three carbene entities forming the plane and the *N*-anchor as well as the terminal imido ligand occupying the pseudo-axial positions (Figure 2, **3**). The crystallographic data reveal remarkably few structural changes upon oxidation of the Co^{III} precursor **2** (Table 1). The one-electron oxidation is accompanied by an *elongation* of the Co–N(imido) bond from 1.677(1) Å in **2** to 1.697(3) Å in **3**, and a significant shortening of the N(imido)–C(mesityl) bond from 1.369(2) Å in **2** to 1.310(5) Å in **3**. Despite the different substituents (aryl vs. alkyl), the Co–N(imido) bond length in **3** is close to the Co=N bond in the Co^{IV} imido complex [(TIMMN^{mes})Co^{IV}(NAd)](OTf)$_2$ (1.702(3) Å).[8n] However, the N(imido)–C(mesityl) bond in **3** (1.310(5) Å) is considerably shorter than that in [(TIMMN^{mes})Co^{IV}(NAd)](OTf)$_2$ (1.405(4) Å). This difference is likely due to electron delocalization within the aryl imido fragments. In contrast to **2**, the *N*-anchor in **3** binds to the cobalt ion (d(Co–N1) = 2.058(3) Å), and, consequently, pulls it deeper into the electron-rich cavity of TIMMN^{mes}. It is noteworthy that the N(imido)–C(mesityl) and C–C bond lengths within the mesityl group of **3** closely resemble those in the previously reported triplet nitrene copper complex, in accord with persistent radical delocalization (Figure 2).[6] Akin to **2**, one of the mesityl groups of the TIMMN^{mes} ligand in **3** is nearly parallel to the mesityl group of the imido ligand, with a centroid-centroid distance of 3.62 Å and an interplanar angle of only 4.57° (in **2**: 3.70 Å, 10.34°), indicating a π–π interaction.[19] Further remarkable is the fact that the Co–N-(imido)–C(mesityl) bond angle of 174.6(3)° in **3** is closer to linearity compared to that in the Co^{III} precursor **2** (158.0-(1)°). The average Co–C bond length of 1.954(3) Å in **3** is similar to the one determined in its precursor **2** (1.943(2) Å), implying that the one-electron oxidation does not greatly affect the Co–C(carbene) interaction. Also worth noting are the short distances between the imido nitrogen (N8) and two of the coordinated carbene carbon (C2, C10) ligands:

Table 1: Summary of important structural parameters of **2** and **3** in the solid-state and as obtained by calculations at the TPSSh–D3/ZORA-def2-SVP level of theory [in brackets].[a]

Parameter	**2**	**3**
d (Co=N8)	1.677(1) Å [1.652 Å]	1.697(3) Å [1.690 Å]
d (Co–N1)	3.236 Å [3.216 Å]	2.058(3) Å [2.077 Å]
d (C40–N8)	1.369(2) Å [1.357 Å]	1.310(5) Å [1.313 Å]
d (N8–C$_{carbene}$)[b]	2.795(3) Å [2.696 Å]	2.553(4) Å [2.521 Å]
av d (Co–C)	1.943(2) Å [1.913 Å]	1.954(3) Å [1.945 Å]
d_{oop} (Co)	0.882 Å [0.657 Å]	0.317 Å [0.487 Å]
∡ (Co–N8–C40)	158.0(1)° [153.7°]	174.6(3)° [174.1°]
Σ(C–N–C)	359.7(2)° [359.4°]	332.5(3)° [337.5°]

[a] A similar fit between experimental and computed structural parameters is obtained with PBE–D3 (Table S7); a more detailed table of metric parameters for complexes **1**–**3** and [(TIMEN^{mes})Co-(NAr^{OMe})]$^+$ [8d] as well as triplet nitrene [(^{EMind}L)Cu(N(C$_6$H$_4$^{t}Bu))]) [6] is given in Table S4. The value d_{oop} denotes the "out-of-plane"-shift, quantifying the distance at which the cobalt atom lies above or below the plane of the three carbene ligands. [b] The shortest distance between the imido nitrogen (N8) and one of the coordinated carbene carbon ligands.

the N8–C10 (2.618 Å) and N8–C2 (2.553 Å) distances are smaller than the sum of their VdW radii (3.25 Å).

The EPR spectrum of **3** (Figure 3) displays an eight-line signal centered at $g_{av} \approx 1.98$ with hyperfine coupling due to the ^{59}Co nucleus ($I = 7/2$, 100 % nat. abundance). The nitrogen super-hyperfine coupling is unresolved. The best simulation of the experimental spectrum was obtained with an effective spin $S = 1/2$, and effective g-values at $g_1 = 2.00$, $g_2 = 1.98$ and $g_3 = 1.95$, with a hyperfine coupling constant of
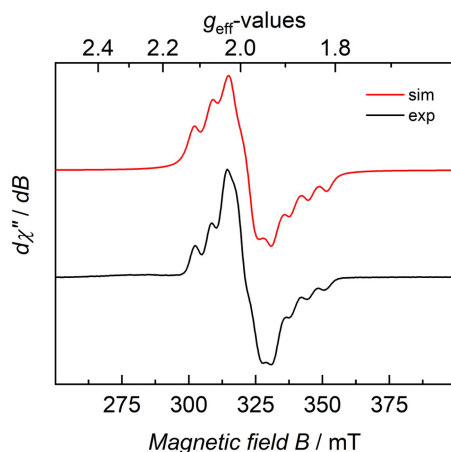

Figure 3. CW X-band EPR spectrum of [(TIMMN^{mes})Co(NMes)](PF$_6$)$_2$ (**3**), recorded as a 5 mM frozen THF solution at 6 K (black trace), and its simulation (red trace). Experimental conditions: microwave frequency $\nu = 8.959$ GHz, modulation width $= 0.01$ mT, microwave power $= 1.0$ mW, modulation frequency $= 100$ kHz, time constant $= 0.1$ s. Simulation parameters: effective spin $S = 1/2$, effective g-values $g_1 = 2.00$, $g_2 = 1.98$ and $g_3 = 1.95$, linewidths $W_{FWHM,1} = 7.00$ mT, $W_{FWHM,2} = 12.0$ mT and $W_{FWHM,3} = 3.00$ mT. Voigt ratios (Lorentz $= 0$, Gauss $= 1$) $V_1 = V_3 = 0.00$; $V_2 = 1.00$. Hyperfine coupling to one ^{59}Co ($I = 7/2$, 100 % nat. abundance) nuclei was determined as $A_3 = 63.5 \times 10^{-4}$ cm^{-1} (6.79 mT).
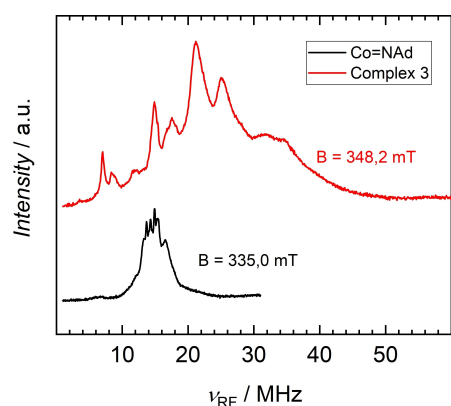
Figure 4. Davies ENDOR spectra recorded at 9.70 GHz on [(TIMMN^{mes})Co^{IV}(NAd)](OTf)$_2$ (black trace) and [(TIMMN^{mes})Co-(NMes)](PF$_6$)$_2$ (**3**) (red trace). Experimental conditions (for black spectrum): $T = 10$ K, $B = 335.0$ T, MW ($\pi/2$) $= 100$ ns, prep (π) $= 200$ ns, $\tau = 400$ ns, RF pulse $= 8$ μs, repetition time $= 1$ ms, 2 h acquisition time. Experimental conditions (for red spectrum): $T = 10$ K, $B = 348.2$ mT, MW ($\pi/2$) $= 100$ ns, prep (π) $= 200$ ns, $\tau = 400$ ns, RF pulse $= 8$ μs, repetition time $= 1$ ms, 2 h acquisition time.

$A_3 = 63.5 \times 10^{-4}$ cm^{-1} (6.79 mT). Computational analysis using the TPSSh functional reproduces the experimental values well ($g_1 = 1.99$, $g_2 = 1.98$, $g_3 = 1.96$, $A_3 = 53 \times 10^{-4}$ cm^{-1} (5.67 mT). The small hyperfine coupling constant is more similar to those for the putative Co^{III} mono- imidyl/nitrene radicals[11,12] than to those reported for Co^{IV} imido complexes.[8n,9] This and the g-values near 2 suggest that there likely is a significant amount of imido ligand-centered spin density in **3**. ENDOR studies were performed for **3** and the previously published tetravalent Co imido [(TIMMN^{mes})Co^{IV}(NAd)](OTf)$_2$[8n] for comparison (Figure 4, Figure S36). The spectrum of the Co^{IV}NAd complex (black) spans a relatively narrow frequency range of roughly 10 to 20 MHz with all signals being symmetric around the proton Zeeman frequency (Table S2). The bands in the ENDOR spectrum of **3** (red) are also symmetric around the proton Zeeman frequency, but now span a range of 6 to 24 MHz (Table S3). The increased spectral width indicates that the unpaired electron is effectively closer to the ligand, giving rise to larger proton hyperfine couplings in **3** as compared to Co^{IV}NAd. In addition, a very broad signal is present in the ENDOR spectrum of **3** that spans a range from 0 to 45 MHz with a maximum intensity at 33 MHz. As compared to the calculated ^{14}N hyperfine couplings of -8, 2 and 52 MHz, the ^{14}N ENDOR signal under neglect of quadrupole contributions would be expected in the range of 0 to 26 MHz. The intensity maximum at 33 MHz is reasonably close to 26 MHz and, thus, the broad signal is tentatively assigned to nitrogen. We conclude that EPR and ENDOR spectroscopic data as well as structural parameters for **3** substantiate a ligand-centered oxidation of **2**; and thus, favor the formulation of **3** as a cobalt-imidyl radical with a metal oxidation state of +III. Despite multiple attempts, and due to the pronounced thermal instability, reliable SQUID magnetization data were not obtained for **3**.

To provide further support for the formulation of **3** as a cobalt-imidyl radical, high-energy resolution Kα-detected X-ray absorption spectroscopy (HERFD XAS) was performed at the Co K-edge. Complexes **2** and **3** were measured (Figure 5), together with [(TIMMN^{mes})Co^{II}(Cl)](PF$_6$), [(TIMMN^{mes})Co^{III}(NAd)](BPh$_4$), and [(TIMMN^{mes})Co^{IV}-(NAd)](OTf)$_2$ as references with known electronic structures (see Supporting Information, Figures S37–S41). The pre-edge region is characterized by a main peak in the 7708–7712 eV region, due to 1s to 3d transitions, and a weaker feature at 7713–7716 eV, associated with 1s to ligand π* transitions. The first moment of the 1s to 3d pre-edge transitions in **2** and **3** are at nearly the same energies, indicative of both cobalt centers having similar effective nuclear charges. There are, however, changes in the 1s to ligand π* transition energies, which may be attributed to the low-lying tricarbene π* molecular orbitals experiencing greater destabilization in **3**. In addition, there are differences in the rising edge, which likely reflect some anisotropy in the electronic donation within the x, y and z axes of the molecules. However, as observed in the pre-edge region, the average edge energies are similar and accordingly disfavor a metal-based oxidation in **3**.
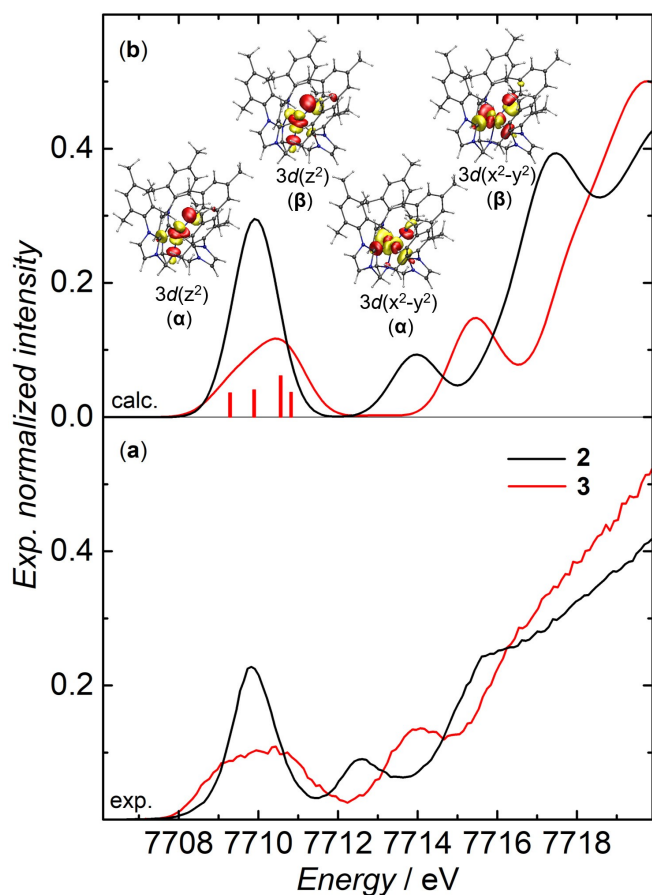
Figure 5. Experimental Co K-edge HERFD XAS (a) and TDDFT calculated spectra (b) with key natural transition orbitals[21] of the dication in **3** associated from left to right with the pre-edge peak transitions shown as red sticks. Energy shift: +93.2 eV; scale factor: 0.11; line shape: Gaussian; FWHM: 1.3 eV.

The strong agreement between experiment and theory (Figure 5, Figures S37–S41 in the Supporting Information) lends credence to the interpretation of the experimental data within the TDDFT framework.[21,22] The pre-edge peak of **2** is dominated by transitions to orbitals with strong Co $d(xz)$ and $d(yz)$ character, which are antibonding combinations with N^{mes} $2p$ orbitals lying perpendicular and parallel to the mesityl plane, respectively (Figure S40). The higher intensity in **2** results from the larger Co $4p$ admixture (2–4 % vs. 1–2 % in **3**), as a consequence of an electric dipole mechanism. Interestingly, the formal Co $d(z^2)$ acceptor orbital in the first two excited states of **3** has a strong N^{mes} $2p$ character, reaching 28 % in the transition of the first β electron. The analogous excitation in **2** has only 17 % N^{mes} character. This indicates that the low-energy side of the pre-edge peak of **3** is largely a transition from Co 1s to N-radical bearing a spin-up electron; thus, further corroborating the imidyl assignment. Lastly, the high-energy side (3rd and 4th excited states) is mainly due to excitation into cobalt's $d(x^2-y^2)$ orbital, in which the acceptor orbitals have 49–51 % total d- and only 3–4 % N^{mes} character. In summary, the XAS data and TDDFT calculations of **3** are consistent

with a closed-shell Co^{III} ion bound to an imidyl radical ligand.

Further quantum chemical analysis at the CASSCF level was carried out. The cobalt ion in **2** features doubly occupied $d(z^2)$, $d(xy)$, $d(x^2-y^2)$ orbitals and; hence, is best described with a cobalt +III oxidation state (Figure 6). The shape and position of the d-orbitals, which are not aligned with the coordinate system, indicate a sizable pseudo-Jahn–Teller effect.[23] The bonding with the imido ligand via the two metal-centered π-interactions (Co:N = 0.3:0.7; Löwdin's population analysis), is moderately covalent. Thus, the electronic structure of **2** is to be understood as a mesomerically stabilized and nucleophilic imide-type complex, as is also indicated by the bent imido linkage in the solid-state structure. Geometry optimization using the PBE functional and a truncated ligand system (substituting Mes for Me) likewise predicts a bent Co=N–C linkage (156°). This confirms that the bending of the imido group is an intrinsic feature pertinent to the underlying electronic structure.

One-electron oxidation of **2** to **3** does not simply remove an electron from the HOMO, the $d(z^2)$ orbital, as had been obtained for the adamantyl congener.[8n] Instead, the ligand-centered (Co:N = 0.2:0.8), antibonding π*-orbital, which is mesomerically stabilized by the mesityl substituent (i.e., iminyl electronic structure), is populated by one electron in **3** (Figure 7). This weakens the Co–N(imido) bond and explains its counterintuitive elongation upon oxidation. In
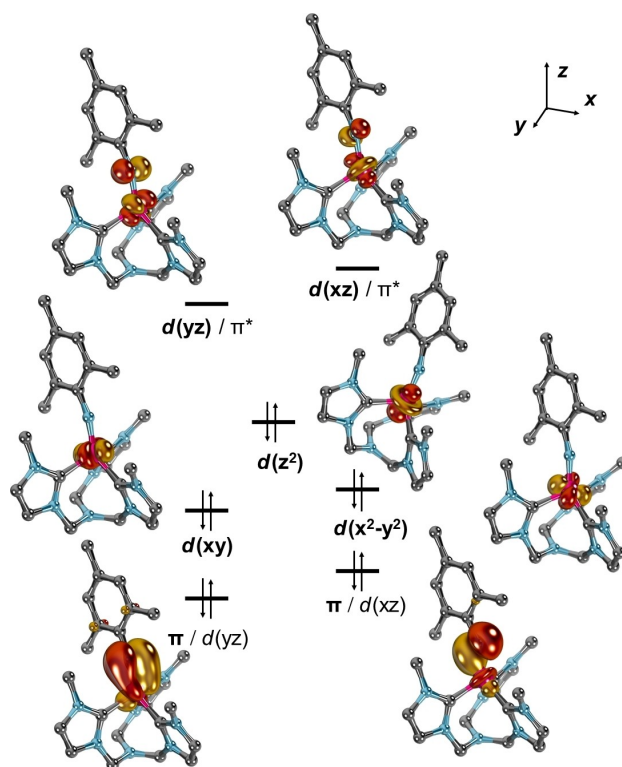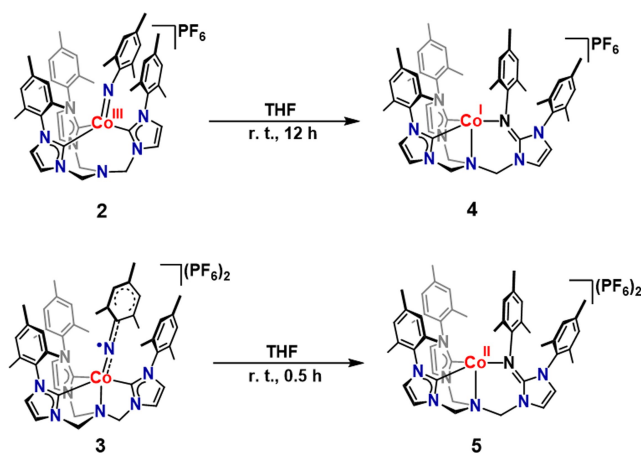

Figure 6. Electronic structure of the ground state of the cation in **2** according to CASSCF(10,7) calculations ($c = 0.82$; Figure S56). Sequence and spacing of the orbitals have been chosen for clarity and do not reflect their energies. Hydrogen atoms and mesityl substituents of the NHC ligands are omitted for clarity in this Figure.
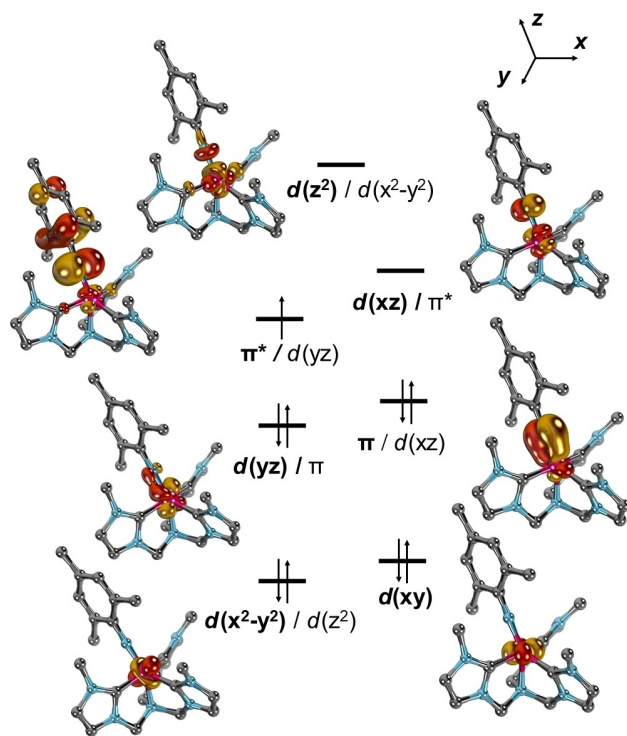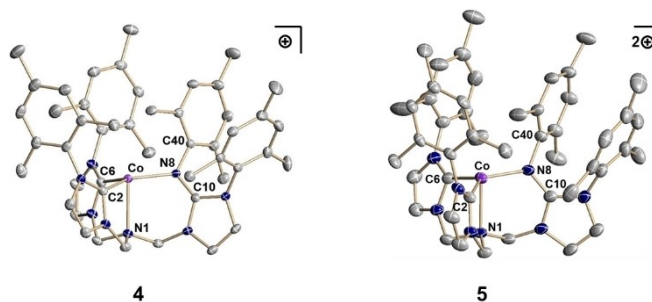
Figure 7. Electronic structure of the ground state of the dication in **3** according to CASSCF(11,8) calculations ($c = 0.84$). Sequence and spacing of the orbitals have been chosen for clarity and do not reflect their energies. Ligand-centered bonding combinations regarding the approximated $d(z^2)/d(x^2-y^2)$ orbitals (Figure S58), hydrogen atoms, and mesityl substituents of the NHC ligands are omitted for clarity.

Scheme 2. Intramolecular migratory insertion reactions by complexes **2** and **3**.

Figure 8. Molecular structures of the cation in crystals of [(TIMMN^{mes})-*Co^I(NMes)′](PF$_6$)·C$_6$H$_6$ (**4**), and dication in crystals of [(TIMMN^{mes})-*Co^{II}(NMes)′](PF$_6$)$_2$·CH$_2$Cl$_2$ (**5**); hydrogen atoms and solvent molecules were omitted for clarity. Thermal ellipsoids are displayed at 50% probability.

perfect agreement, Löwdin's population analysis corroborates a spin density of 0.6 a.u. at the imido nitrogen atom and a comparatively low Co–N bond order of BO = 1.4 (**2**, BO = 1.8). Accordingly, the Co–N–C angle increases upon oxidation, in line with a +III oxidation state of the metal and a radical imido ligand. Note that the coordination of the tertiary amine N1 to the cobalt ion in **3** switches the coordination geometry from four-coordinate, distorted seesaw geometry in **2**, to five-coordinate distorted, trigonal-bipyramidal in **3**; thus, flipping the frontier orbitals.

The isolation of the cobalt imido/imidyl redox pair provides a unique opportunity to compare their *N*-group transfer reactivities without affecting the metal center's oxidation state. While **2** is stable in the solid-state at room temperature and in solution at −35°C, stirring a THF solution of **2** at ambient temperature overnight led to the slow formation of the *N*-heterocyclic imine[24] [(TIMMN^{mes})-*Co^I(NMes)′](PF$_6$) (**4**) (Scheme 2, top). Complex **4** was characterized by SC-XRD analysis (Figure 8) as well as UV/Vis electronic absorption and IR vibrational spectroscopy (Figures S13, S14), SQUID magnetometry (Figure S15), and CHN elemental analysis. This type of intramolecular imido insertion reaction has been observed before for the related Co^{III} imido TIMEN derivative [(TIMEN^{mes})Co-(NAr^{OMe})]$^+$.[8d] In the TIMEN ligand system, the proposed intermediate, namely a Co^I imine, is too unstable to be isolated and further disproportionates to the Co^{II} imine

[(TIMEN^{aryl})*Co(NAr)′]$^{2+}$, metallic Co^0, and unidentified organic byproducts.[8d]

In the molecular structure of cation **4**, the modified TIMMN* ligand coordinates the cobalt ion through two of its remaining NHCs, the anchoring nitrogen atom, and the newly formed imine. In the IR spectrum of **4**, the characteristic vibration of the imino group is observed at 1562 cm^{-1} (Figure S13). Variable-temperature (VT) and variable-field (VF) SQUID measurements of **4** revealed a magnetic moment (μ_{eff}) of 3.10 μ_B at 300 K; thus, supporting the high-spin $S = 1$, Co^I, d^8 electronic structure assignment (Figure S15).

Unlike the Co^{III} imido **2**, the isostructural imidyl **3** is considerably more reactive, transforming at room temperature in solution and even in the solid-state. In THF solution at room temperature, the imidyl **3** quantitatively rearranges to the Co^{II} imine **5** within 0.5 h (Scheme 2). Complex **5** was also fully characterized, including SC-XRD analysis, featuring a similar coordination geometry as that of complex **4** but with two well-separated PF$_6^-$ counter anions (Figure 8, **5**).[25] As expected for a divalent Co complex, **5** possesses an $S = 3/2$ spin state, which was experimentally validated by X-band EPR spectroscopy (Figure S21) and VT-VF SQUID mag-

netization (Figure S22) and further confirmed by DFT studies (see Supporting Information). VT-VF SQUID measurements of a solid sample of **5** revealed a magnetic moment (μ_{eff}) of 4.35 μ_B at 300 K. The observed room-temperature moment falls within the range of 4.3 μ_B to 4.8 μ_B, which is typical for high spin Co^{II} complexes in pseudo-tetrahedral or lower symmetry,[26] and is suggestive of a quartet spin ground state for **5**. Similar to **4**, the characteristic vibration of the imino group in **5** is centered at 1552 cm^{-1} (Figure S18).

Reactivity studies of **2** and **3** with various reagents, such as styrene, cyclohexene, 1,4-cyclohexadiene, triphenylphosphine, phenyl isocyanate, CS$_2$ as well as CO$_2$ and CO turned out rather unproductive (Scheme S1, Figures S23–S29). However, it is noteworthy that **2** undergoes imido/oxo exchange in reaction with carbon dioxide (CO$_2$) at room temperature to give complicated mixtures of cobalt species and free mesityl isocyanate (MesNCO).

The mechanism for the insertion reactions of **2** and **3** was modeled by DFT calculations.[27] In the case of **2** (Figure 9, top), where the adiabatic singlet/triplet energy gap was calculated to be only $+3$ kJmol^{-1}, spin-crossover occurs prior to the transition state. The calculated barrier for **ts[2→4]^t** of $\Delta G^{\ddagger} = +95$ kJmol^{-1} (**ts[2→4]^s**: $\Delta G^{\ddagger} = +117$ kJmol^{-1}) is in excellent agreement with the experimental value of $\Delta G^{\ddagger} = +94$ kJmol^{-1} ($\Delta H^{\ddagger} = +77$ kJmol^{-1} and $\Delta S^{\ddagger} =$

-57 Jmol^{-1}K^{-1}) as obtained by VT-UV/Vis studies (Figures S31, S32), which further corroborate first order kinetics. For **3** (Figure 9, bottom), spin-crossover to $S=3/2$ occurs after the transition state, which is lower in energy (**ts[3→5]^d**: $\Delta G^{\ddagger} = +74$ kJmol^{-1}; **ts[3→5]^q**: $\Delta G^{\ddagger} = +97$ kJmol^{-1}) than the one located for **2**. VT-UV/Vis studies (Figures S34, S35) revealed for the transformation of **3** to **5** in THF first-order kinetics as well, with $\Delta G^{\ddagger} = +88$ kJmol^{-1}, $\Delta H^{\ddagger} = +47$ kJmol^{-1} and $\Delta S^{\ddagger} = -139$ Jmol^{-1}K^{-1}.

Intrinsic bond orbitals (IBOs; Figures S48–S55)[28] were calculated along the reaction coordinate[29] from **2** to **4** to illustrate the electron flow during this transformation (Figure 10; Figures S53, S54). In agreement with the structure of **2** in the solid-state, the IBO associated with one of the two π-bonds of the imido ligand reveals a weak interaction with the π-acidic $p(z)$ orbital of the electrophilic NHC ligand (Figure 10, top left, 2.70 Å). During the reaction, this orbital transforms into the σ-bond with the incoming NHC (Figure 10, top right, 1.34 Å). Consequently, this intramolecular migratory insertion can be understood as a nucleophilic attack of an imide-type ligand on the NHC. The two electrons associated with the lone pair of the NHC migrate to the metal-centered $d(z^2)$ orbital (Figure 10, bottom); thus, formally reducing the metal by two electrons. The π-bond within the *N*-heterocyclic imine ligand is derived from the second MesN=Co π-bond (Figure S53). On the triplet potential energy surface, homolytic cleavage of the NHC–Co bond (Figure S54) and radical coupling of the imido- and NHC ligand occurs. This is reasonable, since the excitation of **2** ($S=0$) to **2** ($S=1$) involves an imido ligand-to-metal charge transfer; consequently, giving an imidyl radical electronic structure with a one-electron reduced cobalt center.

The shape-changes of the IBOs for the transformation of the imidyl **3** to **5** is substantially different, as illustrated in Figure 11 (Figure S55). There, the electron in the singly-occupied π-orbital migrates towards the metal instead of to the NHC, thereby reducing the cobalt ion by only one

ΔG / kJ mol^{-1}
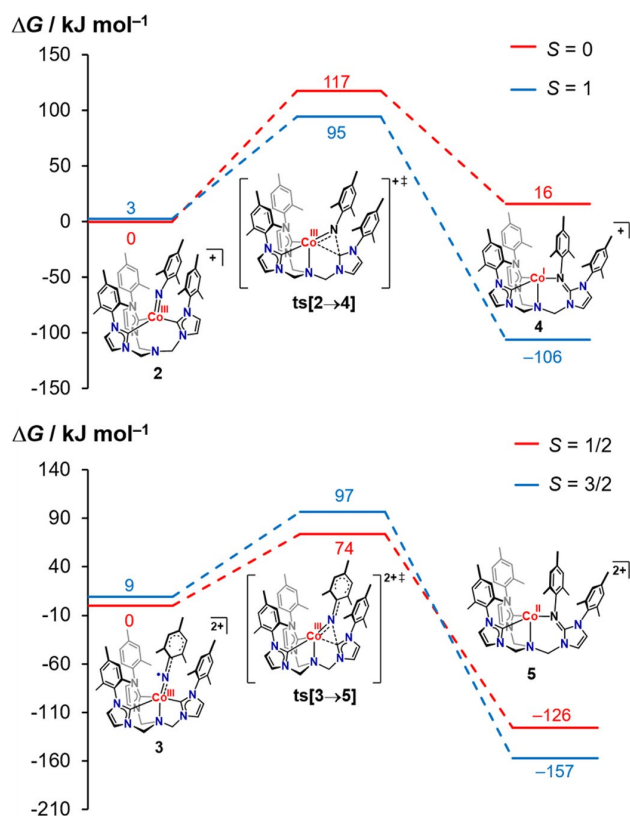
Figure 9. Mechanisms for the insertion reaction of **2** (top) and **3** (bottom), as calculated at the ZORA-TPSSh–D3/def2-TZVPP//ZORA-PBE–D3/def2-SVP level of theory under consideration of solvation in THF.
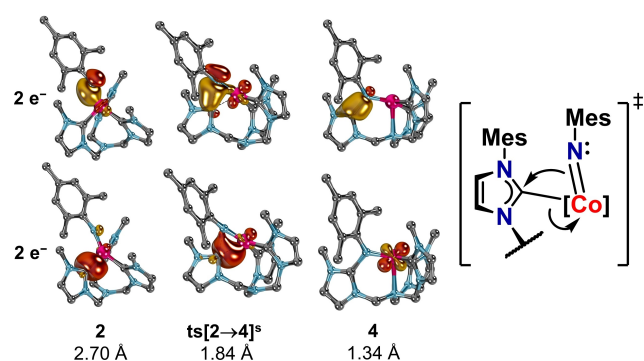
Figure 10. Changes of the IBOs (TPSSh//PBE) associated with one imido-cobalt π-bond (top) and the NHC–Co σ-bond (bottom) along the reaction coordinate (NHC-imido distance given) from **2** to **4** ($S=0$). Spin-crossover occurs close to the transition state, but all orbitals relate to the singlet state for consistency. See Figure S53 for more IBOs along the reaction path and Figure S54 for the triplet potential energy surface.
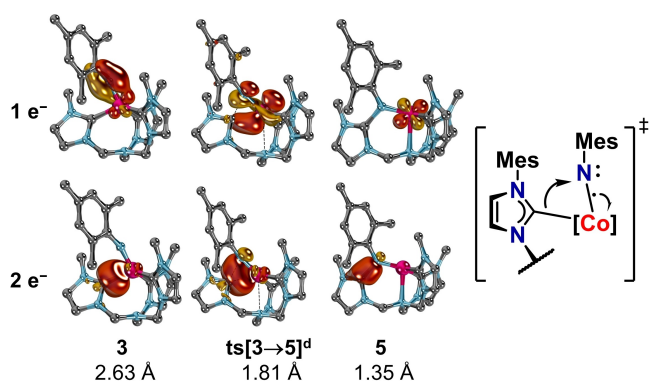
Figure 11. Changes of the IBOs (TPSSh//PBE) associated with the two imido-cobalt π-bonds (top) and the NHC–Co σ-bond (bottom) along the reaction coordinate (NHC–NMes distance given) from **3** to **5** ($S=1/2$). The IBOs obtained at the $S=3/2$ energy surface coincide. See Figure S55 for more IBOs along the reaction path.

electron (Figure 11, top). The formation of the NHC-imine σ-bond is best understood as a nucleophilic attack of the NHC's lone pair (Figure 9, bottom) at an electrophilic imidyl ligand. Note, this NHC lone pair in starting material **3** is already weakly polarized towards the imidyl ligand (Figure 11, bottom left, NHC–NMes = 2.63 Å). This explains the short imidyl-NHC distance observed in the solid-state and the lower reaction barrier in line with the Hammond–Leffler postulate.[30]

Conclusion

In summary, a Co^{III} imido/imidyl complex pair is presented. The rare Co^{III} imidyl title complex [(TIMMN^{mes})Co(NMes)]-(PF$_6$)$_2$ (**3**) was synthesized by oxidation of its Co^{III} imido precursor [(TIMMN^{mes})Co^{III}(NMes)](PF$_6$) (**2**). Diamagnetic precursor **2** features a moderately bent Co–N(imido)–C-(Mes) linkage and EPR, ENDOR, and high-energy X-ray absorption spectroscopy suggest a d^6 low-spin electron configuration for **3** with most of the spin density residing on the ligand. Calculations also indicate a formal oxidation state of $+III$ for both complexes and an imido-type electronic structure for **2**, whereas an imidyl-radical character is found for **3**. Both complexes show intramolecular migratory insertion of the imido ligand into one Co–NHC bond. For **2**, the computational analysis substantiates a mechanism based on the *nucleophilic attack of the* imide onto the electrophilic NHC ligand, whereas **3** reacts by *nucleophilic attack of the NHC onto an electrophilic imidyl-radical* ligand. Thus, oxidation of **2** to **3** facilitates coupling reactions by a switch of mechanism through umpolung of the imido ligand.

Acknowledgements

Conflict of Interest

The authors declare no conflict of interest.

Data Availability Statement

The data that support the findings of this study are available in the Supporting Information of this article.

[1] a) P. Müller, C. Fruit, *Chem. Rev.* **2003**, *103*, 2905–2919; b) L. Zhang, L. Deng, *Chin. Sci. Bull.* **2012**, *57*, 2352–2360; c) K. Shin, H. Kim, S. Chang, *Acc. Chem. Res.* **2015**, *48*, 1040–1052; d) P. F. Kuijpers, J. I. van der Vlugt, S. Schneider, B. de Bruin, *Chem. Eur. J.* **2017**, *23*, 13819–13829; e) Y. Park, Y. Kim, S. Chang, *Chem. Rev.* **2017**, *117*, 9247–9301; f) Y. Liu, T. You, H. X. Wang, Z. Tang, C. Y. Zhou, C. M. Che, *Chem. Soc. Rev.* **2020**, *49*, 5310–5358; g) R. A. Eikey, M. M. Abu-Omar, *Coord. Chem. Rev.* **2003**, *243*, 83–124; h) J. F. Berry, *Comments Inorg. Chem.* **2009**, *30*, 28–66; i) C. T. Saouma, J. C. Peters, *Coord. Chem. Rev.* **2011**, *255*, 920–937; j) K. Ray, F. Heims, F. F. Pfaff, *Eur. J. Inorg. Chem.* **2013**, 3784–3807; k) A. Grünwald, S. S. Anjana, D. Munz, *Eur. J. Inorg. Chem.* **2021**, 4147–4166.
[2] M. J. T. Wilding, D. A. Iovan, A. T. Wrobel, J. T. Lukens, S. N. MacMillan, K. M. Lancaster, T. A. Betley, *J. Am. Chem. Soc.* **2017**, *139*, 14757–14766.
[3] a) E. R. King, E. T. Hennessy, T. A. Betley, *J. Am. Chem. Soc.* **2011**, *133*, 4917–4923; b) D. A. Iovan, T. A. Betley, *J. Am. Chem. Soc.* **2016**, *138*, 1983–1993.
[4] a) Y. Park, S. P. Semproni, H. Zhong, P. J. Chirik, *Angew. Chem. Int. Ed.* **2021**, *60*, 14376–14380; *Angew. Chem.* **2021**, *133*, 14497–14501; b) A. Reckziegel, M. Kour, B. Battistella, S. Mebs, K. Beuthert, R. Berger, C. G. Werncke, *Angew. Chem. Int. Ed.* **2021**, *60*, 15376–15380; *Angew. Chem.* **2021**, *133*, 15504–15508.
[5] Y. Dong, J. T. Lukens, R. M. Clarke, S. L. Zheng, K. M. Lancaster, T. A. Betley, *Chem. Sci.* **2020**, *11*, 1260–1268.
[6] K. M. Carsch, I. M. DiMucci, D. A. Iovan, A. Li, S. Zheng, C. J. Titus, S. J. Lee, K. D. Irwin, D. Nordlund, K. M. Lancaster, T. A. Betley, *Science* **2019**, *365*, 1138–1143.

[7] a) J. Du, L. Wang, M. Xie, L. Deng, *Angew. Chem. Int. Ed.* **2015**, *54*, 12640–12644; *Angew. Chem.* **2015**, *127*, 12831–12835; b) Y. Liu, J. Du, L. Deng, *Inorg. Chem.* **2017**, *56*, 8278–8286; c) X. Yao, J. Du, Y. Zhang, X. Leng, M. Yang, S. Jiang, Z. Wang, Z. Ouyang, L. Deng, B. Wang, S. Gao, *J. Am. Chem. Soc.* **2017**, *139*, 373–380.

[8] a) D. M. Jenkins, T. A. Betley, J. C. Peters, *J. Am. Chem. Soc.* **2002**, *124*, 11238–11239; b) T. A. Betley, J. C. Peters, *J. Am. Chem. Soc.* **2003**, *125*, 10782–10783; c) X. Dai, P. Kapoor, T. H. Warren, *J. Am. Chem. Soc.* **2004**, *126*, 4798–4799; d) X. Hu, K. Meyer, *J. Am. Chem. Soc.* **2004**, *126*, 16322–16323; e) D. T. Shay, G. P. Yap, L. N. Zakharov, A. L. Rheingold, K. H. Theopold, *Angew. Chem. Int. Ed.* **2005**, *44*, 1508–1510; *Angew. Chem.* **2005**, *117*, 1532–1534; f) M. P. Mehn, S. D. Brown, D. M. Jenkins, J. C. Peters, J. L. Que, *Inorg. Chem.* **2006**, *45*, 7417–7427; g) R. E. Cowley, R. P. Bontchev, J. Sorrell, O. Sarracino, Y. Feng, H. Wang, J. M. Smith, *J. Am. Chem. Soc.* **2007**, *129*, 2424–2425; h) C. Jones, C. Schulten, R. P. Rose, A. Stasch, S. Aldridge, W. D. Woodul, K. S. Murray, B. Moubaraki, M. Brynda, G. La Macchia, L. Gagliardi, *Angew. Chem. Int. Ed.* **2009**, *48*, 7406–7410; *Angew. Chem.* **2009**, *121*, 7542–7546; i) E. R. King, G. T. Sazama, T. A. Betley, *J. Am. Chem. Soc.* **2012**, *134*, 17858–17861; j) B. Wu, R. Hernandez Sanchez, M. W. Bezpalko, B. M. Foxman, C. M. Thomas, *Inorg. Chem.* **2014**, *53*, 10021–10023; k) Y. Baek, T. A. Betley, *J. Am. Chem. Soc.* **2019**, *141*, 7797–7806; l) Y. Baek, E. T. Hennessy, T. A. Betley, *J. Am. Chem. Soc.* **2019**, *141*, 16944–16953; m) A. Reckziegel, C. Pietzonka, F. Kraus, C. G. Werncke, *Angew. Chem. Int. Ed.* **2020**, *59*, 8527–8531; *Angew. Chem.* **2020**, *132*, 8605–8609; n) W. Mao, D. Fehn, F. W. Heinemann, A. Scheurer, D. Munz, K. Meyer, *Angew. Chem. Int. Ed.* **2021**, *60*, 16480–16486; *Angew. Chem.* **2021**, *133*, 16616–16622.

[9] L. Zhang, Y. Liu, L. Deng, *J. Am. Chem. Soc.* **2014**, *136*, 15525–15528.

[10] a) V. Lyaskovskyy, A. I. Suarez, H. Lu, H. Jiang, X. P. Zhang, B. de Bruin, *J. Am. Chem. Soc.* **2011**, *133*, 12264–12273; b) M. Goswami, V. Lyaskovskyy, S. R. Domingos, W. J. Buma, S. Woutersen, O. Troeppner, I. Ivanovic-Burmazovic, H. Lu, X. Cui, X. P. Zhang, E. J. Reijerse, S. DeBeer, M. M. van Schooneveld, F. F. Pfaff, K. Ray, B. de Bruin, *J. Am. Chem. Soc.* **2015**, *137*, 5468–5479.

[11] L. Nurdin, D. M. Spasyuk, W. E. Piers, L. Maron, *Inorg. Chem.* **2017**, *56*, 4157–4168.

[12] N. P. van Leest, M. A. Tepaske, J. H. Oudsen, B. Venderbosch, N. R. Rietdijk, M. A. Siegler, M. Tromp, J. I. van der Vlugt, B. de Bruin, *J. Am. Chem. Soc.* **2020**, *142*, 552–563.

[13] Y. Baek, A. Das, S. L. Zheng, J. H. Reibenspies, D. C. Powers, T. A. Betley, *J. Am. Chem. Soc.* **2020**, *142*, 11232–11243.

[14] a) P. Cui, V. M. Iluc, *Chem. Sci.* **2015**, *6*, 7343–7354; b) Y. Xia, D. Qiu, J. Wang, *Chem. Rev.* **2017**, *117*, 13810–13889.

[15] a) F. Ragaini, A. Penoni, E. Gallo, S. Tollari, C. Li Gotti, M. Lapadula, E. Mangioni, S. Cenini, *Chem. Eur. J.* **2003**, *9*, 249–259; b) N. P. Mankad, P. Müller, J. C. Peters, *J. Am. Chem. Soc.* **2010**, *132*, 4083–4085; c) J. A. Bellow, M. Yousif, A. C. Cabelof, R. L. Lord, S. Groysman, *Organometallics* **2015**, *34*, 2917–2923; d) M. Yousif, D. Wannipurage, C. D. Huizenga, E. Washnock-Schmid, N. J. Peraino, A. Ozarowski, S. A. Stoian, R. L. Lord, S. Groysman, *Inorg. Chem.* **2018**, *57*, 9425–9438;

e) S. S. Kurup, D. Wannipurage, R. L. Lord, S. Groysman, *Chem. Commun.* **2019**, *55*, 10780–10783; f) J. M. Andjaba, C. J. Rybak, Z. Wang, J. Ling, J. Mei, C. Uyeda, *J. Am. Chem. Soc.* **2021**, *143*, 3975–3982; g) D. Wannipurage, S. S. Kurup, S. Groysman, *Organometallics* **2021**, *40*, 3637–3644.

[16] D. J. Tindall, C. Werle, R. Goddard, P. Philipps, C. Fares, A. Fürstner, *J. Am. Chem. Soc.* **2018**, *140*, 1884–1893.

[17] a) M. R. Anneser, G. R. Elpitiya, J. Townsend, E. J. Johnson, X. B. Powers, J. F. DeJesus, K. D. Vogiatzis, D. M. Jenkins, *Angew. Chem. Int. Ed.* **2019**, *58*, 8115–8118; *Angew. Chem.* **2019**, *131*, 8199–8202; b) Q. Liu, L. Long, P. Ma, Y. Ma, X. Leng, J. Xiao, H. Chen, L. Deng, *Cell Rep. Phys. Sci.* **2021**, *2*, 100454.

[18] a) L. Yang, D. R. Powell, R. P. Houser, *Dalton Trans.* **2007**, 955–964; b) D. Rosiak, A. Okuniewski, J. Chojnacki, *Polyhedron* **2018**, *146*, 35–41.

[19] C. Janiak, *J. Chem. Soc. Dalton Trans.* **2000**, 3885–3896.

[20] N. D. Harrold, G. L. Hillhouse, *Chem. Sci.* **2013**, *4*, 4011–4015.

[21] F. Plasser, M. Wormit, A. Dreuw, *J. Chem. Phys.* **2014**, *141*, 024106.

[22] S. DeBeer George, T. Petrenko, F. Neese, *J. Phys. Chem. A* **2008**, *112*, 12936–12943.

[23] a) G. E. Cutsail III, B. W. Stein, D. Subedi, J. M. Smith, M. L. Kirk, B. M. Hoffman, *J. Am. Chem. Soc.* **2014**, *136*, 12323–12336; b) M. Keilwerth, L. Grunwald, W. Mao, F. W. Heinemann, J. Sutter, E. Bill, K. Meyer, *J. Am. Chem. Soc.* **2021**, *143*, 1458–1465.

[24] a) X. Wu, M. Tamm, *Coord. Chem. Rev.* **2014**, *260*, 116–138; b) T. Ochiai, D. Franz, S. Inoue, *Chem. Soc. Rev.* **2016**, *45*, 6327–6344.

[25] Deposition Numbers 2131812 (for **1**), 2131813 (for **2**), 2131814 (for **3**), 2131815 (for **4**), 2131816 (for **5**), and 2166115 (for **6**, cf. Supporting Information, Reactivity Studies) contain the supplementary crystallographic data for this paper. These data are provided free of charge by the joint Cambridge Crystallographic Data Centre and Fachinformationszentrum Karlsruhe Access Structures service.

[26] D. M. Jenkins, A. J. Di Bilio, M. J. Allen, T. A. Betley, J. C. Peters, *J. Am. Chem. Soc.* **2002**, *124*, 15336–15350.

[27] Various computational approaches were evaluated (cf. Supporting Information, Computational Details), among which the ZORA-TPSSh-D3(SMD = THF)/def2-TZVPP//ZORA-BP86-D3/def2-SVP level of theory evolved to be in best agreement with the experimentally determined barriers.

[28] G. Knizia, *J. Chem. Theory Comput.* **2013**, *9*, 4834–4843.

[29] a) L. Nunes dos Santos Comprido, J. E. M. N. Klein, G. Knizia, J. Kästner, A. S. Hashmi, *Angew. Chem. Int. Ed.* **2015**, *54*, 10336–10340; *Angew. Chem.* **2015**, *127*, 10477–10481; b) J. E. M. N. Klein, G. Knizia, *Angew. Chem. Int. Ed.* **2018**, *57*, 11913–11917; *Angew. Chem.* **2018**, *130*, 12089–12093.

[30] a) J. E. Leffler, *Science* **1953**, *117*, 340–341; b) G. S. Hammond, *J. Am. Chem. Soc.* **1955**, *77*, 334–338.